P3D-BRNS v1.0.0: A Three-dimensional, Multiphase, Multicomponent, Pore-scale Reactive Transport Modelling Package for Simulating Biogeochemical Processes in Subsurface Environments

Amir Golparvar[1], Matthias Kästner[2] and Martin Thullner[1,3]

[1] UFZ- Helmholtz Centre for Environmental Research, Department of Environmental Microbiology, Leipzig, Germany

[2] UFZ - Helmholtz Centre for Environmental Research, Department of Environmental Biotechnology, Leipzig, Germany

[3] Federal Institute for Geosciences and Natural Resources (BGR), Hannover, Germany

Correspondence: Amir Golparvar (amir.golparvar@ufz.de)

Formatted: Superscript

Abstract

The porous microenvironment of soil offers various environmental functions which are governed by physical and reactive processes. Understanding reactive transport processes in porous media is essential for many natural systems (soils, aquifers, aquatic sediments or subsurface reservoirs) or technological processes (water treatment, or ceramic and fuel cell technologies). In particular, in the vadose zone of the terrestrial subsurface the spatially and temporally varying saturation of the aqueous and the gas phase leads to systems that involve complex flow and transport processes as well as reactive transformations of chemical compounds in the porous material. To describe these interacting processes and their dynamics at the pore scale requires a well-suited modelling framework accounting for the proper description of all relevant processes at a high spatial resolution. Here we present P3D-BRNS as a new open-source modelling toolbox harnessing the core libraries of OpenFOAM and coupled externally to the Biogeochemical Reaction Network Simulator (BRNS). The native OpenFOAM Volume of Fluid solver is extended to have an improved representation of the fluid-fluid interface. The solvers are further developed to couple the reaction module which can be tailored for a specific reactive transport simulation. P3D-RBNS is benchmarked against three different flow and reactive transport processes; 1) fluid-fluid configuration in a capillary corner, 2) mass transfer across the fluid-fluid interface and 3) microbial growth with a high degree of accuracy. Our model allows for simulation of the spatio-temporal distribution of all bio-chemical species in the porous structure (obtained from μ-CT images), for conditions that are commonly found in the laboratory and environmental systems. With our coupled computational model, we provide a reliable and efficient tool for simulating multiphase, reactive transport in porous media.

1 Introduction

Subsurface environments (soils, aquifers, aqueous sediments) are (typically) porous media host a multitude of biogeochemical processes and interactions and provide different versatile ecosystem functions (e.g. C sequestration, compound degradation, nutrient retention, provision of food, fibers and fuel, habitat for organisms, water retention and purification, etc. (Baveye et al., 2016). These processes are controlled by various biological (e.g., microbial abundance and activity), chemical (e.g., distribution of dissolved and volatile species, mineral composition and surface properties of the solid matrix) and physical (e.g., porous structure and permeability, water saturation) properties of the system. These features create a complex web of interactions, the magnitude and effectiveness of which change dynamically in space and time (Graham et al., 2014). Microbial communities, for example, and their metabolic capacity are considered to be directly related to energy and matter fluxes (Thullner et al., 2007) which are in turn, governed by pore arrangements and their connectivity. Along with other environmental factors this can also modify various properties of the porous media (e.g. by biomass accumulation on pore walls (Thullner, 2010), or mineral dissolution or precipitation (Meakin and Tartakovsky, 2009), which in turn are altering the conditions for biogeochemical processes, too.

In soils (or more generally the vadose zone) the dynamically varying distribution of the aqueous and gaseous phase leads to specifically complex and variable constraints for biogeochemical processes. In the past, obtaining (bio)chemical and microbiological information at the pore level was neither economically nor logistically a feasible option (Baveye et al., 2014). Also for the sake of applicability, traditionally, researchers had more tendency to look for ~~macroscale~~ Darcy-scale solutions to tackle environmental issues (White and Brantley, 2003). The Darcy- scale ~~macroscale~~ view (experimental, theoretical or a mixture of both) serves well the purpose of practical applicability (White and Brantley, 2003), but for example, in the context of microbially mediated degradation processes in the vadose zone, it fails to provide insights on the driving mechanisms, as it overlooks important contributing factors, such as the tortuous porous structure/pathways open to the transport of (bio-)geochemical species, non-uniform distribution of water and air phases, as well as the nonlinear ~~relation~~ dependency between changes of the local nutrient and biomass concentrations and the bulk concentrations of (bio)geochemical species.~~change of in local biomass concentration and the its relation with bulk nutrient concentration~~. Evidence at microscopic level has shown that biological activity and evolution are more locally organized (Kuzyakov and Blagodatskaya, 2015) where Darcy-scale ~~macroscopic~~ studies lead to loss of crucial information. This has motivated the development of sophisticated physics-based models implementing all aspects of hydrological, geochemical and biological processes involved in microbial growth and evolution.

66 Reactive Transport Models (RTMs) are a class of mathematical models that have been applied

67 extensively to study biogeochemical systems for about four decades (Parkhurst and Appelo,

68 1999;Thullner et al., 2005;Thullner and Regnier, 2019;Meile and Scheibe, 2019). There is a long list of

69 principal factors and mechanisms governing biogeochemical reactions at the pore scale. Numerically,

70 these processes can be defined and solved either by fully (global) implicit approaches or by separating

71 and solving different components once at a time. For the continuum scale a wide range of reactive

72 transport models exist which allow for the simulation of biogeochemical processes (Steefel et al., 2015b).

73 In turn, at the pore scale, models combining the simulation of flow, transport and reactive

74 (biogeochemical) processes are scarce, and existing model developments are often driven by specific

75 research questions and/or are subject to severe simplifications in the description of the pore space

76 (Golparvar et al., 2021). Integrated models- explicitly capturing simultaneously the structural properties of

77 the soil at the ~~microscale~~pore -scale, the resulting multiphase flow and multispecies reactive transport are

78 hardly available (Tian and Wang, 2019).

79 Recently, new frontiers of pore-scale RTMs are emerging with the advances in computational power as

80 well as with huge improvements in imaging techniques~~.~~, The latter includes (e.g., ~~in~~ the static and

81 dynamic scanning of porous structure as well of as fluids' distribution (Schlüter et al., 2019) or ~~in~~ the

82 detecti~~onng~~ of bacterial distributions in soil using ~~e.g.,~~catalyzed reporter deposition with fluorescence in

83 situ hybridization (CARD-FISH) technique (Schmidt et al., 2015). Direct Numerical Models (DNMs) are

84 becoming the nexus of next generation of RTMs as they represent the porous structure in a fully explicit

85 manner (directly obtained from soil samples, digitized and fed into RTMs) in addition to offering a more

86 flexible coupling of different components of reactive transport models (Baveye et al., 2018;Raeini et al.,

87 2012;Li et al., 2010;Yan et al., 2016). Another advantage of using DNMs is that they offer a great deal of

88 flexibility in considering settings and conditions that are experimentally impossible to impose (Tian and

89 Wang, 2019).

90 In this work, we introduce the pore-scale RTM package P3D-BRNS explicitly involving the structure and

91 topology of the pore space, the co-existence/co-flow of both the aqueous and the gaseous phase, the

92 advective-diffusive transport of species in each phase, and an arbitrary set of reactive processes controlled

93 by kinetic rate laws or thermodynamic constraints. The fluid flow field is updated via solving the Navier-

94 Stokes (NS) equations (Patankar and Spalding, 1972). The Volume-Of-Fluid (VOF) approach is adopted

95 to account for different phase distribution (Hirt and Nichols, 1981). The transport of chemical species is

96 considered via solving the Advection-Diffusion-Reaction Equation (ADRE), where the concentration

97 jump for soluble/volatile compounds across the fluid/fluid interface is modelled via the Continuous

98 Species Transfer (CST) method (Haroun et al., 2010). Reactive processes are defined and simulated

3

99 externally via coupling the flow and transport model to the BRNS (Biogeochemical Reactions Network

100 Solver) package (Regnier et al., 2002;Aguilera et al., 2005). The model structure is introduced and the

101 model performance is shown and compared with analytical counterparts. The model capabilities are

102 depicted for a fully three-dimensional case.

103 2   Mathematical Formulation

104 The entire numerical domain (Ω) can be decomposed to two main sub-regions: solid space (Ω_S) and void

105 space (Ω_ϑ). The void space is further divided into aqueous phase ($\Omega_{\vartheta,aq}$) and gaseous phase ($\Omega_{\vartheta,gs}$)

106 which are partitioned by the fluid-fluid interface (Ω_I). The overall domain is bounded externally between

107 inlet (Ω_{in}) and outlet (Ω_{out}) boundaries, which allow for inflow/outflow of different phases and chemical

108 species, as well as no-flux boundaries resembling physical walls, where nothing is allowed to leave or

109 enter the domain (Ω_{wall}). The domain is limited internally by no-flow boundaries where solid space and

110 void space intersect (i.e. solid surface, $\Omega_\vartheta \cap \Omega_S = \Omega_{wall}$).

111 2.1   Fluid Flow: Governing Equations

112 Evolution of a single/multi-phase, isothermal, incompressible, immiscible fluid(s) can be expressed by

113 basic conservation principles. These can be formulated into a single-field formalism (Hirt and Nichols,

114 1981):

$$\nabla \cdot \boldsymbol{u} = 0 \qquad in \ \Omega_\vartheta \tag{1}$$

$$\rho \left(\frac{\partial \boldsymbol{u}}{\partial t} + \boldsymbol{u} \cdot \nabla \boldsymbol{u} \right) = -\nabla P + \nabla \cdot \tau + \rho g + F_\sigma \qquad in \ \Omega_\vartheta \tag{2}$$

115 where $\boldsymbol{u}$ is the vector of velocity field, $\boldsymbol{\rho}$ is the fluid density, $\boldsymbol{P}$ is the pressure, $\boldsymbol{g}$ is the gravitational

116 vector, and $\boldsymbol{\tau}$ is the stress tensor which can be defined as $\tau = 2\mu S = 2\mu(0.5[(\nabla \boldsymbol{u}) + (\nabla \boldsymbol{u})^T])$ with $\boldsymbol{\mu}$ as

117 the fluid viscosity. $\boldsymbol{F_\sigma}$ denotes the interfacial tension force, which is nonzero only when two or more

118 phases (excluding solid) are available. It is safe in using the incompressible form of the Navier-Stokes

119 equation for low Mach and Reynolds numbers

120 In case of simultaneous flow of two different phases (~~e.g. flow of air and water under unsaturated conditions~~

121 ~~–~~Figure 1: Illustration of a porous medium at the pore scale with one fluid invading the other (on the left).

122 Mathematical representation of the phase saturation in the computational cells around the interface (on

123 the right). The dashed line shows the actual location of the interface while values in each cells show the

124 amount of water saturation relevant to topology of the dashed line. Black dots represent volatile

125 compounds able to cross the fluid-fluid interface; green dots represent non-volatile compounds restricted

4

126 to the transport in the aqueous phase.Figure 1), their locations and distribution are represented via

127 introducing an indicator function, $\boldsymbol{\alpha}$, taking values within the range $[0, 1]$. The first continuous fluid is

128 marked as $\alpha = 1$, the second fluid is denoted as $\beta = 1 - \alpha$ and for the transition from one fluid to the other

129 (i.e. the interface, Ω_I), α varies between 0 and 1. Fluid density and viscosity in each grid cell is then

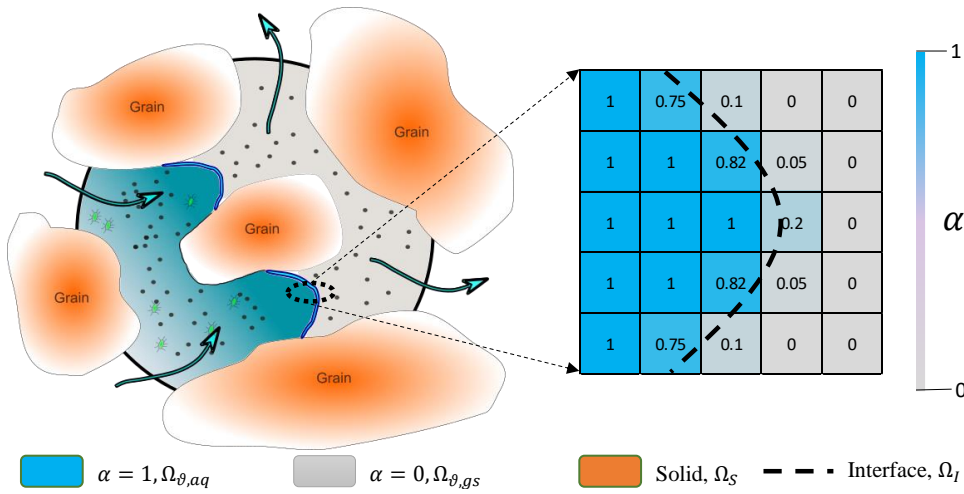130 calculated from a linear interpolation of this indicator function:

$$\rho = \alpha \rho_1 + (1 - \alpha)\rho_2 \qquad in \; \Omega_\vartheta \tag{3}$$
$$\mu = \alpha \mu_1 + (1 - \alpha)\mu_2 \qquad in \; \Omega_\vartheta \tag{4}$$

131 A mass conservative boundary condition at the fluid-fluid interface is written as:

$$\llbracket \rho_i (\boldsymbol{u}_i - w) \cdot n_{\Omega_I} \rrbracket = 0 \qquad in \; \Omega_I \tag{55}$$

132

Figure 1: Illustration of a porous medium at the pore -scale microscale with one fluid invading the other (on the left). Mathematical representation of the phase saturation in the computational cells around the interface (on the right). The dashed line shows the actual location of the interface while values in each cells show the amount of water saturation relevant to topology of the dashed line. Black dots represent volatile compounds able to cross the fluid-fluid interface; green dots represent non-volatile compounds restricted to the transport in the aqueous phase.

133 with ρ_i as the density of ith fluid, $\boldsymbol{u}_i$ as the velocity of ith fluid, w as the velocity of the interface, n_{Ω_I} as

134 the normal vector to the interface (Ω_I) pointing from the invading phase to the displaced one and the

135 brackets showing the jump condition at the interface. Individual velocities, $\boldsymbol{u}_i$, and the interface velocity

136 w, are not directly calculated but furthermore averaged to derive the global mass conservation equation

137 that is used for numerical discretization (for full derivation, consult with (Graveleau et al., 2017)).

138   In the context of the Finite Volume Method (FVM), discretization of the physical domain produces a
139   finite subset of discrete volumes (taking the shape of a polyhedral). The key implication of the Volume of
140   Fluid method is to define and solve for global variables, rather than having one equation for each variable
141   in each phase. Hence, the idea is to transform the integro-differential equations into their global versions
142   by averaging them over each cell volume (Whitaker, 2013). For multiphase systems, after a few steps of
143   linearization and approximation (see Hirt and Nichols (1981) for a detailed derivation), the Volume of
144   Fluid formulation of the momentum equation (2)(2) is obtained as:

$$\rho\left(\frac{\partial \overline{\boldsymbol{u}}}{\partial t} + \overline{\boldsymbol{u}} \cdot \nabla \overline{\boldsymbol{u}}\right) = -\nabla P + \nabla \cdot \mu(\nabla \overline{\boldsymbol{u}} + (\nabla \overline{\boldsymbol{u}})^t) + \rho g + F_\sigma \qquad in\ \Omega_\vartheta \qquad (6)(6)$$

Formatted: Font:

145   with having $\overline{\boldsymbol{u}}$ as the global averaged velocity vector. For the sake of simplicity, we drop the "average"
146   notation from the global velocity vector (i.e. will refer to $\overline{\boldsymbol{u}}$ as $\boldsymbol{u}$), for the rest of this paper. The pressure
147   gradients (and Reynolds numbers) considered in our simulations are in the range that render changes in
148   the gas compressibility negligible.

149   Since we are dealing with only two fluids, index i in $\boldsymbol{u}_i$ takes only two values; α and β - one for each
150   phase. A global, mass conservative, advection equation is used to describe the evolution of the indicator
151   function:

$$\frac{\partial \alpha}{\partial t} + \nabla \cdot (\alpha \boldsymbol{u}) + \nabla \cdot (\alpha(1-\alpha)\boldsymbol{u_c}) = 0 \qquad in\ \Omega_\vartheta \qquad (7)$$

152   where α indicates the volume fraction of phase 1, $u_c = u_\alpha - u_\beta$ is the vector of the compressive velocity
153   with $u_{\alpha,\beta}$ as velocity vector of phase α and β right on the edge of the interface (detailed explanation on
154   deriving eq. (7)(7) can be found in the Supplementary Information**Error! Reference source not found.**-).
155   ~~The latter term in equation (7) is active only in the presence of an interface.~~ It is derived from mass
156   conservation equation written for phase α, which computationally helps with maintaining
157   stiffness/sharpness of the interface. Sharpening interface means having the interface span over a fewer
158   number of computational grids. u_c is the vector of compressive velocity on each face of all computational
159   grids. Since we don't solve for the velocity field of each phase individually, a direct calculation of u_c is
160   not possible. However, we can rather take an indirect approach for computing u_c as follows:

$$\boldsymbol{u}_c = min\big(c_\alpha|\boldsymbol{u}|, max(|\boldsymbol{u}|)\big)\frac{\nabla \alpha}{|\nabla \alpha|} \qquad in\ \Omega_I \qquad (8)$$

161   In equation (8)(8), c_α is a compression coefficient providing some level of control over how wide the
162   interface spans. The max function operates on the magnitude of unit velocity vector calculated on all the
163   faces of a computational grid. To counteract the numerical diffusion and avoid the spread of interface
164   over several computational grids, values of $c_\alpha > 1$ provide an enhanced/sharper interface. A where a

6

165 value of $c_\alpha = 0$ gives no compression of the interface, ~~whereas values of $c_\alpha > 1$ provide an~~
166 ~~enhanced/sharper interface~~ (Graveleau et al., 2017). In simulation scenarios introduced in this paper, c_α
167 has been assigned the value of 1, <u>unless stated otherwise</u>~~unless otherwise is stated~~.

168 To calculate the interfacial tension force, $\boldsymbol{F_\sigma}$, (Brackbill et al., 1992) have introduced a Continuum
169 Surface Force (CSF) which requires computing the curvature of the interface:

$$\kappa = \nabla . n_{\Omega_I} \qquad in\ \Omega_I \tag{9}$$

170 with having κ as mean interface curvature <u>in each computational grid</u>, and n_{Ω_I} as the interface unit
171 normal vector defined as:

$$n_{\Omega_I} = \frac{\nabla\alpha}{|\nabla\alpha|} \qquad in\ \Omega_I \tag{10}$$

172   Given the curvature, the interfacial tension force can be ~~computed~~ <u>approximated</u> as:

$$F_\sigma = \sigma\kappa\nabla\alpha \qquad in\ \Omega_I \tag{11}$$

173 where σ is the surface tension between two fluids <u>(derivation of this approximation can be found in</u>
174 <u>Brackbill et al., 1992)</u>.

175 2.2   Reactive Transport: Governing Equations

176 Concentrations of mobile species are affected by advection (i.e. transport with the moving fluid),
177 molecular diffusion and reactive transformation. Also, in case of having two fluids simultaneously in the
178 system, different species can cross the fluid-fluid interface, causing local fluctuations in concentration
179 values. In general to account for all the changes in species concentrations, the ADRE for biogeochemical
180 reactive components can be written as:

$$\frac{\partial C_i}{\partial t} + \nabla \cdot (C_i\boldsymbol{u}) = -\nabla \cdot \left(J_{d,i} + J_{m,i}\right) + R_i \qquad in\ \Omega_\vartheta \tag{12}$$

181 where $J_{d,i}$ is the molecular diffusive flux of component i, $J_{m,i}$ is the mass flux of component i due to mass
182 transfer across the fluid-fluid interface and R_i accounts for the changes in concentration of component i
183 due to reactions. Molecular diffusion follows Fick's law:

$$J_{d,i} = -D_i\nabla(C_i) \qquad in\ \Omega_\vartheta \tag{13}$$

184 where D_i is the diffusion coefficient of species i. At the interface, the assumption of thermodynamic
185 equilibrium implies equality of chemical potentials. Given the condition that liquid concentration of
186 component i is proportional to the partial pressure of the species in the secondary phase (e.g. gas, oil or
187 minerals), a partitioning relationship such as Raoult or Henry's law (Danckwerts and Lannus, 1970) can
188 be established to relate species concentrations on both sides of the interface:

$$C_{i,\beta} = H_i C_{i,\alpha} \qquad in \ \Omega_I \tag{14}$$

189 with $C_{i,\alpha}$ as concentration of species i in phase α, H_i as Henry's constant of species i and $C_{i,\beta}$ as

190 concentration of species i in phase β. Depending on if a given compound's concentration in the aqueous

191 phase or the gaseous phase is multiplied by the Henry's coefficient, (14)(14), the definition of Henry's

192 constant switches between the solubility or volatility for that compound (i.e. $H_i^{soluility} = \left.1\middle/H_i^{volatility}\right.$)

193 (Sander, 2015). Unless otherwise stated, the volatility concept of Henry's law is adopted in order to

194 define the concentration relationship of a given compound across the fluid-fluid interface (14)(14). The

195 concentration field around the fluid-fluid interface (where $\nabla\alpha \neq 0$) at equilibrium, for any values of $H \neq$

196 1, is discontinuous which imposes the additional flux, $J_{m,i}$, to satisfy the concentration jump across the

197 interface. Hence the mass transfer flux, $J_{m,i}$, can be derived within the VOF framework (i.e. CST) as

198 follows (Haroun et al., 2010):

$$J_{m,i} = -D_i \frac{1 - H_i}{\alpha + (1 - \alpha)H_i} C_i \nabla\alpha \qquad in \ \Omega_\vartheta \tag{15}$$

199 It is noteworthy that few assumptions and volume averaging methods are implemented to derive equation

200 (15)(15), which readers are encouraged to check the references for more details. The diffusion coefficient

201 is calculated from harmonic interpolation:

$$D_i = \frac{1}{\dfrac{\alpha}{D_{i,A}} + \dfrac{1 - \alpha}{D_{i,B}}} \qquad in \ \Omega_\vartheta \tag{16}$$

202 where $D_{i,\alpha-\beta}$ is the diffusion coefficient of species i in phase α and β respectively.

203 Simulated reactions include kinetically as well as thermodynamically constrained reactions. For a

204 kinetically constrained reaction j the reaction rate $r_j = f(C_1, ..., C_n)$ is needed while for a

205 thermodynamically constrained reaction k the equilibrium conditions defined by a law of mass action

206 $M_k=f(C_1, ..., C_n)$ is needed with M_k as equilibrium constant. These equations can be of arbitrary form and

207 the resulting reaction network defines the term R_i in equation (12)(12) (Aguilera et al., 2005;Regnier et al.,

208 2002). For immobile species concentration changes are only due to reactive processes.

209 2.3   Boundary Conditions (BCs)

210 There are various types of boundary conditions, corresponding the real physical conditions, most of which

211 can be derived from two basic types:

8

212   •   Dirichlet boundary (fixed value) which relates the value of a variable at a given geometric
213   location to a constant value; e.g. $C_i = 1M$ in Ω_{in} meaning a constant 1 molar concentration of
214   component i at the boundary,
215   •   von Neumann boundary (fixed gradient) which provides the value of a variable's gradient at the
216   face of the boundary cell; e.g. $\partial_n p = 0$ in Ω_{wall} giving a zero pressure gradient on the wall.

217 In general, our model can apply any of these basic boundary conditions to any scalar or vector variables
218 such as pressure, velocity/flux, concentration of volume of fluid fields, but one needs to assure that the
219 imposed BC(s) are both compatible and they reflect the correct physical boundary conditions. For
220 example, for velocity/flux-pressure coupling, a Dirichlet (i.e. constant) boundary for flux at the inlet can
221 be coupled with either 1) fixed discharge velocity/flux and zero gradient (i.e. von Neumann) pressure at
222 both inlet and outlet, or 2) a constant pressure head at the inlet and atmospheric pressure at the outlet with
223 zero gradient velocity/flux at both ends, or 3) fixed values of pressure and velocity/flux at one end and
224 zero gradient at the other end. In the beginning of section 2̲2̶, typical composition and configuration of an
225 arbitrary computational domain is described. Inlet, outlet and impermeable boundaries are amongst the
226 most common types that one might face. Inlet BC means for the direction of fluid flux to be pointing
227 inwards (i.e. into the domain) while for the outlet, the direction of the flux should be outwards. Also for
228 the impermeable wall, zero-orthogonal fluxes need to be satisfied. Either Dirichlet, von Neumann or a
229 mixture of both can be used at a particular boundary. Mathematical translation and implementation of
230 these boundaries are provided in the next section. Time-dependent BCs (e.g. cyclic or seasonal
231 water/species influx) are also readily available to be applied, but never been used in this work. Unless
232 otherwise stated, boundary conditions that have been imposed on each section of the computational
233 domain are described as follows:

234 **At impermeable boundaries (Ω_{wall}):** Physical wall implies no flux perpendicular to the normal vector
235 to its surface. No slip BC is an appropriate BC for the velocity field on the wall. In general, they all can
236 be written as:

$$\partial_n C_i = 0, \quad u_{x,y,z} = 0, \quad \partial_n p = 0, \quad \partial_n \alpha = 0 \quad in \ \Omega_{wall} \tag{17\cancel{17}}$$

237 For the velocity field, on the wall, a slip boundary condition is also available to be applied.

238 **At inlet/outlet boundaries ($\Omega_{in}, \Omega_{out}$):** Concentration of reactants, products and inert tracers are set to
239 fixed values at inlet, while they are allowed to leave the domain at outlet with zero gradient boundary
240 condition. Constant flowrate with zero pressure gradient is applied at inlet and an atmospheric pressure
241 (fixed value) with zero velocity gradient is set at outlet. Also in case of two-phase flow, the invading

9

242 phase is set to enter from inlet at fixed value and exits from outlet with zero gradient BC. Mathematically,

243 they can be expressed as:

$$C_i \geq 0, \quad \boldsymbol{u} = const., \quad \partial_n \boldsymbol{p} = 0, \quad \alpha = const. \quad in \ \Omega_{in} \tag{18}$$

244 together with:

$$\partial_n \boldsymbol{C_i} = 0, \quad \partial_n \boldsymbol{u_n} = 0, \quad \boldsymbol{p} = 0, \quad \partial_n \boldsymbol{\alpha} = 0 \quad in \ \Omega_{out} \tag{19}$$

245 with u_n as the normal velocity vector. While we have mostly applied equations (18) and (19) for

246 designing an inlet/outlet duo, other formats, such as defining a pressure head (plus zero gradient velocity)

247 on the inlet in combination with either constant exit pressure or constant discharge rate, are readily

248 available to implement as well.

249 **At the fluid-fluid-solid contact line** (Ω_{l^3})**:** At the fluid-fluid-solid contact line, in case of no interactions

250 or no reaction of any chemical species with the solid, the boundary condition at the triple point is derived

251 to be:

$$\nabla C_i \cdot \boldsymbol{n_s} = \frac{H_i - 1}{\alpha H_i + (1 - \alpha)} C_i \nabla \alpha \cdot \boldsymbol{n_s} \quad in \ \Omega_I \tag{20}$$

252 with $\boldsymbol{n_s}$ as the normal vector to the solid surface (Graveleau et al., 2017). Also, the concept of contact

253 angle is applied by making the following modification to the interface normal vector:

$$n_{\Omega_{l^3}} = cos\theta \boldsymbol{n_s} + sin\theta \boldsymbol{t_s} \quad in \ \Omega_{l^3} \tag{21}$$

254 where $\boldsymbol{n_s}$ is normal vector and $\boldsymbol{t_s}$ is the tangential vector to the solid surface (Brackbill et al., 1992). At

255 the triple point, i.e. fluid-fluid-solid interface, $n_{\Omega_{l^3}}$ is used for normal vector to the interface. CSF,

256 though, has been reportedly generating non-physical spurious currents (Scardovelli and Zaleski, 1999).

257 For this, many have tried to eliminate/mitigate this issue by explicit representation of the interface either

258 via using the Geometric VOF method (Popinet, 2009) or coupled Level-set (LS) VOF functions

259 (Albadawi et al., 2013). Geometric VOF is quite suitable for structured grids, but for porous structures

260 with highly unstructured grids, the calculations can become quite complicated. Alternatively, Raeini et al.

261 (2012) suggested filtering the capillary forces parallel to the interface, which can significantly reduce the

262 non-physical velocities. In short, the modifications they proposed and which are used here are: 1)

263 smoothing the indicator function to have a better measure of the interface curvature, 2) sharpening the

264 indicator function for computation of the interfacial tension force, 3) filtering the capillary pressure force

265 parallel to the interface, and 4) filtering capillary fluxes based on the capillary pressure gradient (for full

266 description of each point, please consult with (Raeini et al., (2012)).

267 To sum up what has been presented so far, we integrated a) the original *interFoam* solver from the

268 OpenFOAM library that only solves for the advection-diffusion transport of two phase flow, with b)

10

269 the improved-interface-resolver library from Raeini et al. (2012), and ~~added~~ c) added a scalar transport

270 solver on top of them. Finally, the full-scale advection-diffusion-reaction model of the biogeochemical

271 species is attained by coupling this to an external reaction-network solver, which is explained in the

272 section 2.4 below.

273 ## 2.4 Numerical Formulation

274 The mass conservation (eq. (1~~1~~), momentum (NS - eq. (2~~2~~) and indicator function (eq. (7~~7~~) equations are

275 all implemented within the open source computational fluid dynamics (CFD) package, OpenFOAM

276 (Greenshields, 2015). OpenFOAM utilizes the finite volume methodology (FVM), a common choice for

277 CFD problems as FVM works only with conservative flux evaluation at each computational cell's

278 boundaries, making it robust in handling nonlinear transport problems. Also all the differential equations

279 mentioned before are first written in their integral form over each cell volume and then converted to the

280 surface summations using Green's Theorem.

281 ~~In this work, t~~The original two-phase (VOF) flow solver, i.e. *interFoam*, is modified to construct our

282 biogeochemical reactive transport package. The momentum equation (2~~2~~) is linearized in a semi-discrete

283 form as:

$$A_d \boldsymbol{u} = \boldsymbol{H}(\boldsymbol{u}) - \nabla P + \boldsymbol{F}, \qquad\qquad (22\text{~~22~~})$$

284 where A_d holds the diagonal elements of the coefficient matrix, $\boldsymbol{H}(\boldsymbol{u})$ contains off-diagonal elements of

285 the coefficient matrix including all source terms, and $\boldsymbol{F}$ entails any body forces (interfacial tension force

286 only in this case). Temporal discretization is handled via the first order Euler method while spatial

287 discretization is managed via second order finite volume schemes. Convection terms of the momentum

288 equation and indicator function (7)~~(eq. 7)~~ are computed using a bounded self-filtered central differencing

289 (SFCD) scheme (based on Gauss's theorem). Rearranging equation (22)~~(22)~~ for velocity and imposing the

290 continuity equation (1)~~(1)~~, the following linear pressure equation can be obtained:

$$\sum_f \frac{S_f}{\langle A_d \rangle_f} \nabla_f^\perp P = \sum_f \left(\langle \frac{\boldsymbol{H}(\boldsymbol{u})}{A_d} \rangle_f \cdot |S_f| + \frac{\varphi_{F,f}}{\langle A_d \rangle_f} \right). \qquad\qquad (23\text{~~23~~})$$

291 S_f in equation (23)~~(23)~~ denotes the outward area-vector of face f, the notation $\nabla_f^\perp$ shows face normal

292 gradients calculated right on the face centers, $\langle \rangle_f$ shows the interpolated values of a face-centered

293 parameter from its cell-centered counterpart, and $\varphi_{F,f}$ is the interfacial force flux term.

294 The velocity-pressure coupling of equations (1)~~(1)~~ and (2)~~(2)~~ are solved using Pressure Implicit with

295 Splitting of Operators (PISO) (Issa, 1986). PISO embodies a predictor-corrector strategy to

296 simultaneously update pressure and velocity within each time step. The resultant system of equations are

11

Formatted: Font:

Formatted: Font:

Formatted: Font:

Formatted: Font:

297 solved on the cell faces and then interpolated back to calculate velocities and pressure at the cell centers.

298 The coupling of indicator function (eq. (7)7) and momentum equation is explicitly defined and solved

299 right after the PISO step is finished. Within the same time step, transport and reaction of different species

300 are then solved sequentially – using a Sequential Non-Iterative Algorithm (Steefel et al., 2015a;Steefel

301 and MacQuarrie, 1996). Time step size is controlled by introducing a Courant number. Time is discretized

302 using either Euler or Crank-Nicholson methods and spatial discretization is performed using the Van Leer

303 second order Total Variation Diminishing scheme (TVD) (van Leer, 1979).

304 The reaction network is built separately and externally solved within the BRNS package - which employs

305 first order Taylor series expansion terms and uses Newton-Raphson method to iteratively solve the

306 system of linear equations (Regnier et al., 2002). BRNS utilizes MAPLE programming language to

307 construct the Jacobian matrix (which contains the partial derivatives of unknown parameters, i.e.

308 concentrations) and other problem-related data such as rate parameters and translating them to a

309 FORTRAN package. The FORTRAN code is then compiled to generate shared object (*.so file) that can

310 be dynamically called later from the transport solver (Centler et al., 2010). The significance of having

311 dynamically shared object file is more apparent when running computationally-demanding

312 cases/scenarios while decomposing and running the application in parallel. BRNS is invoked once the

313 new concentrations are computed from the transport solver. The updated concentrations from the BRNS

314 library (i.e. updating concentrations from redox reactions) are then fed back into the transport solver

315 before moving to the next time step. This process repeats until the final time is reached. This coupling

316 scheme has been successfully used for other RTM approaches before (Centler et al., 2010;Gharasoo et al.,

317 2012;Nick et al., 2013). As the reactions are localized, the reaction solver is modular, and OpenFOAM

318 inherently provides parallelized simulations (via domain decomposition), the P3D-BRNS can easily be

319 used to model larger systems. To achieve higher performance, it is recommended to utilize physical cores

320 than using hyper-threading. The parallelization of our model strengthen its scalability in the sense of the

321 size (pore scale or Darcy scale) of the simulated system. However, in terms of upscaling (e.g., from the

322 pore scale to the Darcy scale) an intermediate step would be required depending on the complexity of the

323 processes that are involved and on the size of the domain.

324 Prior to run simulations, the physical settings of the domain are required to be specified; i.e. the physical

325 geometry of the pore space with proper boundaries and the meshing scheme should be designed.

326 OpenFOAM provides a basic utility for defining boundaries as well as mesh generation which are

327 translatable by the OpenFOAM engine. Any other meshing software/freeware can be freely used as long

328 as an OpenFOAM-compatible format for the meshed file can be created. The overall workflow required

329 to build and run a case/scenario is summarized in Figure 2Figure 2.

Formatted: Font: Times New Roman, Not Bold, Complex Script Font: Not Bold

330
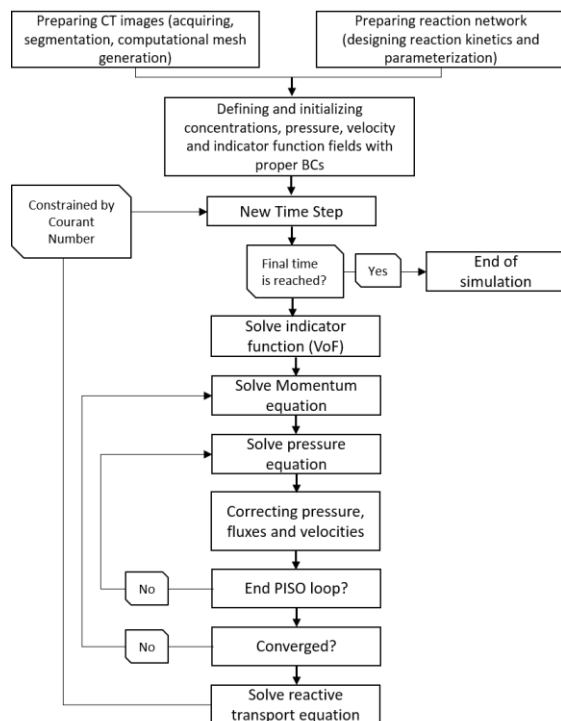
Figure 2: Full solution procedure to simulate a reactive transport process at its fullest complexity.

3   Model Performance

The presented reactive transport model is designed 1) to capture real world pore structures in up to three dimensions, 2) to explicitly simulate the transient distribution of a gas and a liquid phase within the entire pore space and 3) to simulate a full set of advection-diffusion-reaction mechanisms. Capturing the correct curvature of the interface depends heavily on the grid resolution. For a fixed velocity magnitude, higher grid resolution, enforces shorter time-step size (from Courant number) for the numerical simulations to converge. ~~T~~Also ~~t~~o validate different features of the model various simplified scenarios were used which allow the use of analytical expressions as reference for the numerical results. We here show three representative test scenarios addressing different features of the model (two-phase flow, mass transfer across the fluid-fluid interface and reactive transport) individually. Subsequently, the model capabilities are depicted in a final biodegradation scenario making use of the various model features simultaneously.

13

3.1 Fluid Configurations

In order to test our model's performance in simulating two-phase flow, we have zoomed into a two-dimensional porous structure and isolated only one single corner taking the shape of an equilateral triangle. A triangulated mesh is adopted that naturally conforms to the overall shape of the domain. Initially, two immiscible fluids (one wetting, and one non-wetting, e.g. water and air) are placed in such a way that their interface forms a straight line (Figure 3Figure 3, a). The side length of the triangle is 1 mm with a mesh size of 1 µm. Under thermodynamic equilibrium conditions, the force exerted by the pressure difference between two phases is countered by the interfacial tension force. This, along with the contact angle of the non-wetting phase at the wall surface in presence of the wetting phase (e.g. water), determines the topology of the fluid-fluid interface. For a given corner half-angle, the distance that wetting phase spreads over the solid surface from the corner vertices (the highlighted section with green color on Figure 3Figure 3, b), b, can be calculated as:

$$b = r\frac{\cos(\theta + \beta)}{\sin(\beta)} \tag{2424}$$

with r as the radius of the interface's curvature, θ as the contact angle and β as the corner half-angle (Blunt, 2017). In order to reach thermodynamic equilibrium, we performed transient, two-phase flow simulations to compute velocity, pressure and indicator function fields until the triple contact line (Ω_{l^3}) is static. For this, we first divided the equilateral triangle in half, as the problem is symmetrical along the height of the triangle. The symmetrical plane implies that there is no gradient (of any scalar or vector field) perpendicular to its surface while the tangential components (of all fields) remain the same. To find the fluid configuration at equilibrium, we simulated the two-phase flow scenario in two steps. First, we applied a closed boundary condition on the bottom domain by setting $\boldsymbol{u} = 0$ together with $\partial_n p = 0$. Also a closed boundary is imposed on the topmost part of the domain which follows the same BC as the bottom. This way, the interface is able to reconfigure and reorient itself in order to recreate the imposed contact angle with the wall, and at the same time, pressure is allowed to build up in both phases to support the shape of the interface. Then, in order to obtain an equilibrium curvature for the interface, bottom and top domains are opened. This is achieved by setting the 1) pressure in Ω_{in} to the average pressure within the non-wetting phase, 2) pressure in Ω_{out} to the average pressure within wetting phase together with 3) $\partial_n \boldsymbol{u} = 0$ on both Ω_{in} and Ω_{out}. At this stage, we applied a special BC for the indicator function to allow the fluids to enter or leave the domain at both ends, so that the interface can freely transition to its static shape. At the inlet (Ω_{in}), the BC for α is set to switch between $\partial_n \alpha = 0$, if the fluid flux is pointing outwards, and $\alpha = 0$ if the fluid flux is directed into the domain. Also at the outlet (Ω_{out}), the BC for α switches between $\boldsymbol{\alpha} = 1$, if the fluid flux is inwards, and $\partial_n \boldsymbol{\alpha} = 0$, if the fluid flux is outwards. This

374   ensured that appropriate fluids entered the domain from either inlet or outlet boundaries. The radius of

375   curvature can be also evaluated from the Young-Laplace equation ($P_c = \frac{\sigma}{r}$). With a pressure difference of

376   255.33 (kg m^{-1} s^{-2}) obtained from the last step and a surface tension of 0.07 (kg s^{-2}), the radius of

377   curvature is calculated to be 2.17e-4 m. In a different approach, once the interface attains stationarity, we

378   calculated r for equation (24)(24) as the reciprocal of the interface's mean curvature (2.77e-4 m). For a

379   contact angle of 10° and a corner half-angle of 30°, the analytically calculated value for the length, b, of

380   the section in contact with the wetting phase is 375 µm, while the numerical solution yields 370 µm.

381   With a relative error of 1.21% this shows a reasonable match between numerical and analytical solutions

382   in modelling two-phase flow.

383

(a)   (b)
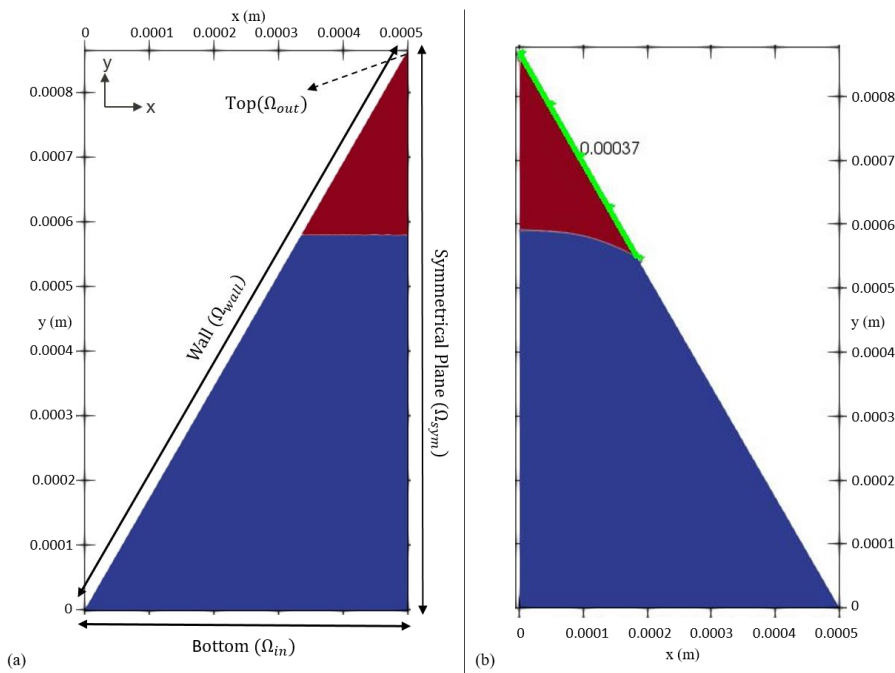
384   **Figure 3**: Initial condition (a) versus final arrangement (b) of the two phases in the fluid configurations scenario. The blue color
385   indicates the non-wetting and the red color shows the wetting phases respectively. The dashed arrow shows the location of the
386   outlet, while the solid-line arrows depict the extent of others boundaries. Once equilibrium is reached (figure b), the curvature of
387   the interface corresponds to the force balance between pressure difference across the interface and the surface tension which can
388   be used to verify the model's sanity. The distance of the contact point (i.e. the point/line where all three phases – water, air and
389   solid – meets) from the corner vertex (highlighted as green), also provides another measure for checking the accuracy of the
390   numerical model.

15

391 ### 3.2 Mass Transfer across the Fluid-Fluid Interface

392 Mass transfer of dissolved species between different phases~~,~~ is particularly of importance for various
393 biogeochemical processes in unsaturated subsurface environments ~~as e.g., oxygen or volatile organic~~
394 ~~carbon compounds are found in the liquid and the gas phase, yet their transport and reaction conditions~~
395 ~~differ highly between these two phase~~such as highly volatile contaminated water streams.

396 Model performance in simulating mass flux across the fluid-fluid interface is validated via a numerical
397 experiment in which two immiscible stationary fluids (an aqueous - α - and a gaseous - β - phase, $\mathbf{u} = 0$ in
398 Ω_ϑ) are horizontally (to remove buoyancy effects) residing on a one dimensional tube of 10 mm length
399 with mesh size of 100 µm. The general partial differential equation (PDE) of equation (12~~12~~) takes the
400 form of a simple diffusive transport as:

$$\frac{\partial C_{tr,i}}{\partial t} - D_{tr,i}\nabla\left(C_{tr,i}\right) = 0 \qquad i = aq, gs$$

$$BC-1: \quad C_{tr,aq} \times H = C_{tr,gs} \qquad in\ \Omega_I \tag{25\cancel{25}}$$

$$BC-2: \quad D_{tr,aq}\frac{\partial C_{tr,aq}}{\partial x} = D_{tr,gas}\frac{\partial C_{tr,gs}}{\partial x} \qquad in\ \Omega_I$$

401 with C_{tr} as the concentration of a volatile tracer and $D_{tr,i}$ as the diffusivity of the tracer in phase *i*. Each
402 phase is set to occupy half of the total volume (Figure 4~~Figure 4~~-a). The system is initialized with a
403 volatile chemical species of concentration of 1 mol m^{-3} in $\Omega_{\vartheta,aq}$, and 0 mol m^{-3} in $\Omega_{\vartheta,gs}$. At the inlet and
404 the outlet boundary, tracer concentration equals that of the nearest solution such that, in short simulation
405 time, it yields no concentration gradient into or out of the domain. The tendency of the dissolved chemical
406 component to cross the fluid-fluid interface is expressed using a constant Henry coefficient. Tracer
407 diffusivity is set to be 1e-5 m^2 s^{-1} in both phases. The analytical solution for equation (25)~~(25)~~ can be
408 found in Bird ~~(Bird,~~ 2002~~)~~.

409 Three scenarios with low, neutral, and high affinity of the volatile compound towards the gaseous phase
410 are considered with corresponding Henry coefficients of 0.01 (low volatility, similar to naphthalene), 1
411 (moderate volatility, e.g., vinyl chloride) and 100 respectively (high volatility, e.g. heptane). For a low
412 value of *H* (*H* = 0.01 – Figure 4~~Figure 4~~-b) little (almost no) tracer is crossing the interface, while at
413 neutral condition (*H* = *1* – Figure 4~~Figure 4~~-c), tracer diffusion is invariant to the phase it is occupying.
414 Evidently for high values of *H* (*H* = *100* – Figure 4~~Figure 4~~-d), significant reduction in the tracer amount
415 within the liquid phase, accompanied by a notable change in concentration across the interface, can be
416 detected. This complies fully with the concentration jump ~~due to~~for ~~the~~such ~~having~~highly volatile
417 component ~~in~~between the liquid and the gas p~~a~~hase. ~~strong depletion of the tracer in aqueous phase as~~

16

418 ~~well as the concentration jump across the interface are observed.~~ The numerical results are ubiquitously
419 identical to the results of the analytical solution (Figure 4~~Figure 4~~-b, c, d). The effect of grid
420 size/resolution is also investigated for this scenario. With 10 times higher grid resolution, the total CPU-
421 elapsed time is increased from ~650 seconds to ~3500 seconds.

422 The concentration profile remains unchanged, but, the average residuals of the numerical solution of the
423 concentration field, calculated at the end of the simulation, is increased from 3.1e-10 to 6.5e-10 (meaning
424 increasing resolution does not necessarily helps with numerical convergence).

425 ~~Also, the average residuals of the numerical solution of the concentration field, calculated at the end of~~
426 ~~the simulation, is increased from 3.1e-10 to 6.5e-10 (meaning increasing resolution does not necessarily~~
427 ~~helps with numerical convergence).~~
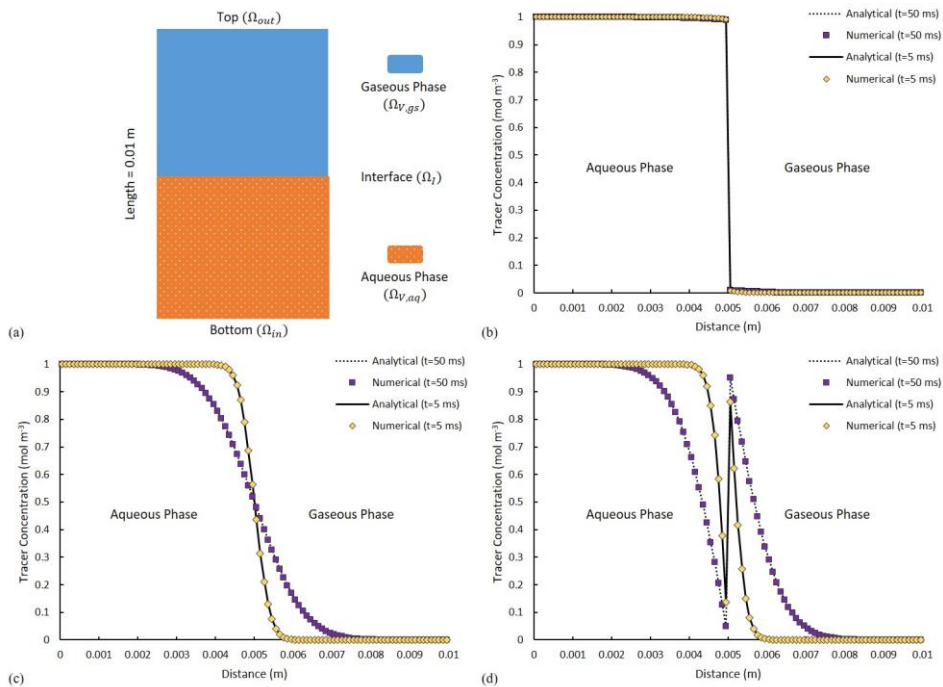
428

429 **Figure 4**: (a) A schematic of the fluid distributions at initial condition. The solid and dotted lines show the analytical solutions
430 with purple and yellow squares depicting the numerical solutions. Comparison of the analytical and numerical solutions of tracer
431 distribution at two distinct time points of t_1=5ms and t_2=50ms for (b) $H = 0.01$, (c) $H = 1$, and (d) $H = 100$.

432

3.3 Microbial Growth and Reactive Transport

Our modelling framework can parameterize any type of reactions, we put the main focus in this subsection on microbially driven redox transformations (i.e. a type of reactions commonly encountered in soils and other porous media environments) and on the implementation of the corresponding mathematical formulation. To validate our model with a scenario in which bacterial biomass is allowed to evolve (i.e. to grow and to decay) we adapted a conceptual biodegradation scenario from (Cirpka and Valocchi, 2007b) in which a fully-water-saturated, two-dimensional ~~domain~~ channel is subjected to a constant flux of two different components; ED (electron donor – e.g. hydrocarbon) and EA (electron acceptor – e.g. oxygen). The imposed uniform flow field is assumed to be constant over time and has only the x-component. The bacteria residing in the channel, faciltiate the reaction between ED and EA, which can be written in an abstract form as $f_a ED + f_b EA \xrightarrow{biomass} f_c Prod$, where $biomass$ is the microbial biomass, $Prod$ is the product(s) (e.g. metabolites such as carbon dioxide) and $f_a, f_b \text{ and } f_c$ are stochiometric coefficients. Assuming a double-Monod kinetics for expressing microbial growth and the microbially driven reaction rates, as well as assuming none of the reactants nor products are involved in secondary reactions, the ADRE (eq. (12)~~12~~) for each chemical species can then be written as:

$$\frac{\partial C_{ED}}{\partial t} + \boldsymbol{u}\frac{\partial C_{ED}}{\partial x} - D_t\frac{\partial^2 C_{ED}}{\partial y^2} = -\frac{C_{ED}}{C_{ED}+K_{ED}}\frac{C_{EA}}{C_{EA}+K_{EA}}\frac{\mu_{max}}{Y}f_a C_{bio} \qquad in\ \Omega_\vartheta$$

$$\frac{\partial C_{EA}}{\partial t} + \boldsymbol{u}\frac{\partial C_{EA}}{\partial x} - D_t\frac{\partial^2 C_{EA}}{\partial y^2} = -\frac{C_{ED}}{C_{ED}+K_{ED}}\frac{C_{EA}}{C_{EA}+K_{EA}}\frac{\mu_{max}}{Y}f_b C_{bio} \qquad in\ \Omega_\vartheta$$

$$\frac{\partial C_{Prod}}{\partial t} + \boldsymbol{u}\frac{\partial C_{Prod}}{\partial x} - D_t\frac{\partial^2 C_{Prod}}{\partial y^2} = \frac{C_{ED}}{C_{ED}+K_{ED}}\frac{C_{EA}}{C_{EA}+K_{EA}}\frac{\mu_{max}}{Y}f_c C_{bio} \qquad in\ \Omega_\vartheta$$

$$\frac{\partial C_{bio}}{\partial t} = \frac{C_{ED}}{C_{ED}+K_{ED}}\frac{C_{EA}}{C_{EA}+K_{EA}}\mu_{max}C_{bio} - \lambda C_{bio} \qquad in\ \Omega_\vartheta$$

(26~~26~~)

where $\boldsymbol{u}$ is the velocity (which has only a constant x-component), D_t is the transverse dispersivity, C_{ED}, C_{EA}, C_{Met} and C_{bio} are concentrations of $ED, EA, Prod$ and $biomass$ respectively; K_{ED} and K_{EA} are half saturation constants for respective compounds in the biomass growth term, Y is the yield coefficient, μ_{max} is the maximum bacterial growth rate, and λ is the bacterial decay rate. Using these equations Cirpka and Valocchi (2007a) developed an analytical solution for steady-state conditions, which in the version of Cirpka and Valocchi (2009) is used as reference for the numerical results.

The numerical experiment is designed to have ED and EA, occupying 25% and 75% of the inlet repectively, and, simultaneously, invading the domain under a constant uniform velocity field, with concentration of C_{ED}^{inlet} and C_{EA}^{inlet}. In a real-world scenario, this can be seen as a plume of a contaminant

18

457 (i.e. a hydrocarbon as ED) being carried into the domain within an oxygenated stream and essentially we

458 are interested in knowing the final concentration/distribution of all bio-chemical species within the

459 domain. The parameters used in this scenario are summerized in Table 1Table 1. Transient reactive

460 transport simluations simulations are perfomed until a steady state is achieved. For validation, we analyze

461 all concentration profiles along the y-axis at a fixed distance of x =2 m and compare them with the

462 analytical solutions. The analytical and numerical results show an almost perfect agreement (Figure

463 5Figure 5, b-e).

Formatted: Font: Times New Roman

Formatted: Font: Times New Roman, Not Bold, Complex Script Font: Not Bold

464
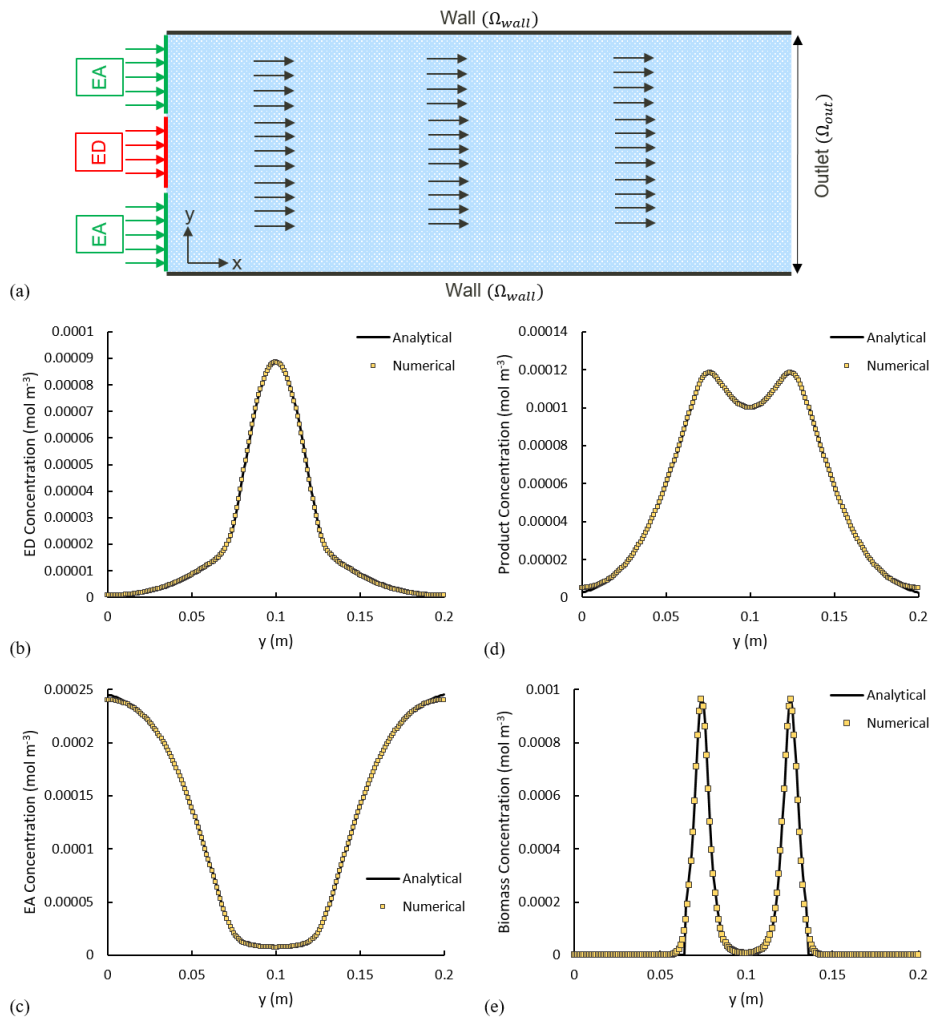
Figure 5: (a) Model set up. The arrows show the direction of the flow field. Solid lines show the analytical solution and the yellow squares illustrate the numerical results. (b-e) Comparison of the analytical and numerical solutions x=2m for concentration of (b) $Electron\ Donor$, (c) $Electron\ Acceptor$, (d) $Product$, and (e) $Biomass$.

468

469

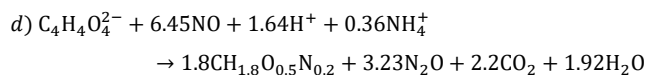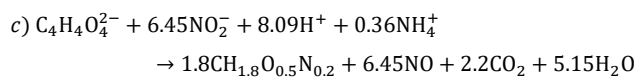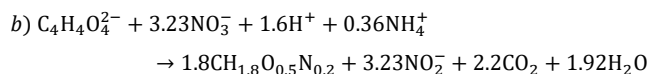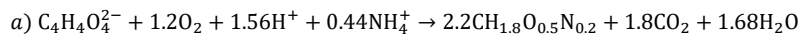Table 1: Parameter values used for simulating microbial growth.

Parameter	Value	Unit	Parameter	Value	Unit
u	100	$cm\ d^{-1}$	μ_{max}	1	d^{-1}
Domain width	20	cm	Domain length	500	cm
D_t	2.5	$cm^2\ d^{-1}$	λ	0.1	d^{-1}
f_a, f_b, f_c	1	-	K_{ED}	8.33e-2	mM
C_{ED}^{inlet}	0.33	mM	K_{EA}	3.13e-2	mM
C_{EA}^{inlet}	0.25	mM	Y	1	–
Mesh size	0.2	mm			

3.4   Theme: Demonstrating Model Capabilities

The scenarios described above are designed to serve as the sole purpose of creating a baseline for validating the numerical toolbox – simple enough where analytical solutions could exist. Unlike the simplicity introduced in previous sections, simulating soil processes with all of the complexities, though, would require having all the modelling elements to be present. We thus present here a scenario with an unsaturated soil hosting the facultative anaerobic bacteria *Agrobacterium tumefaciens*, which performs aerobic respiration under oxic condition, but switches to denitrification using nitrate, nitrite or nitric oxide under anoxic condition (Kampschreur et al., 2012). This example allows us to show our model capabilities, as it involves 1) the actual micro structure of the soil, 2) unsaturated conditions, and 3) an enzymatic reaction network with limiting/inhibition terms. The microstructure is obtained via subsampling from a larger μ-CT image with voxel size of 6 micron (see Supplementary Information). A two-phase simulation is then performed on the voxelized subsample to obtain the fluxes and phase distribution of air and water within the pore space. For this, the entire domain is initially filled with water and subject to injecting air from the top boundary with constant flux of 0.013 ml h^{-1}. An important note to make here is with a relatively high influx, advection transport acts as the bottleneck for numerical time steps. Hence, reactions are performed at a quite slower pace (i.e. larger time steps roughly estimated around 10 hrs). This separation of processes helps improve the overall run-time of the simulations. Generally, the time step sizes are automatically enforced by the Courant number from the transient advective-diffusive transport equation (with order of 10^{-5} seconds). The biomass is assumed to be non-motile meaning it sticks to the solid surface and shows no planktonic behavior. ~~to be~~its Fluids are allowed to leave the domain from the bottom part (kept at atmospheric pressure) while all the remaining sides are set to be impermeable walls. Once fluid configurations in the domain are stationary, their

21

494 distribution along with the velocity profile are used as basis for the reactive transport simulations (phase

495 distributions can be found in the Supplementary Information). Using succinate ($C_4H_4O_4^{2-}$) as organic

496 carbon substrate to be degraded, a metabolic reaction network is constructed with four microbial

497 degradation pathways each following Monod-type kinetics: 1) aerobic respiration with a nitric oxide (NO)

498 inhibitory term, 2) nitrate (NO_3^-) reduction, 3) nitrite (NO_2^-) reduction and 4) NO reduction, with having

499 oxygen (O_2) as inhibitory element for all denitrification conversions (eq. (27)27). Also three additional

500 equations are considered for the synthesis of the three different enzymes required for degradation

501 processes (eq. (28)28). We consider only one single strain of bacteria (*Agrobacterium tumefaciens*) which

502 has the benefits of performing both aerobic respiration and denitrification. Bacteria are considered to be

503 non-motile with an initial concentration of 0.25 mol m^{-2} and uniformly covering the entire grain surface

504 area. Succinate has its initial concentration in the aqueous phase set at 0.2 *mM* (0 *mM* in the gaseous

505 phase), while all other species have their initial concentrations of 0 *mM* in both aqueous and gaseous

506 phases. Boundary condition for all concentration fields on all boundaries is set to zero gradient except for

507 the inlet boundary (fully saturated with air) - where for oxygen it is set to 0.03567 *mM*, and for all others

508 is set to 0 *mM*. In order to avoid depletion of the nitrate in the system, a nitrate concentration of 0.1 μM

509 (as initial condition) is provided. The complete reaction network can be written as follows (Kampschreur

510 et al., 2012):

$a)$ $C_4H_4O_4^{2-} + 1.2O_2 + 1.56H^+ + 0.44NH_4^+ \rightarrow 2.2CH_{1.8}O_{0.5}N_{0.2} + 1.8CO_2 + 1.68H_2O$

$b)$ $C_4H_4O_4^{2-} + 3.23NO_3^- + 1.6H^+ + 0.36NH_4^+$
$\rightarrow 1.8CH_{1.8}O_{0.5}N_{0.2} + 3.23NO_2^- + 2.2CO_2 + 1.92H_2O$

$c)$ $C_4H_4O_4^{2-} + 6.45NO_2^- + 8.09H^+ + 0.36NH_4^+$ $\qquad\qquad$ (27~~27~~)
$\rightarrow 1.8CH_{1.8}O_{0.5}N_{0.2} + 6.45NO + 2.2CO_2 + 5.15H_2O$

$d)$ $C_4H_4O_4^{2-} + 6.45NO + 1.64H^+ + 0.36NH_4^+$
$\rightarrow 1.8CH_{1.8}O_{0.5}N_{0.2} + 3.23N_2O + 2.2CO_2 + 1.92H_2O$

511 Several assumptions are made for preparing the kinetics of the reactions: 1) reaction rates are limited by

512 the maximum specific uptake rate of succinate and are hence independent of its concentration (Beun et

513 al., 2000), 2) sufficient amount of buffer is added to the solution to keep the pH level constant, 3) three

514 nitrogen reductase enzymes ($\xi_{sat,NOR}$ for NO reduction, $\xi_{sat,NIR}$ for nitrite reduction and $\xi_{sat,NAP}$ for

515 nitrate reduction) can have saturation values varying between 0 (i.e. non-existing) and 1 in a bacterial cell,

516 and 4) inhibitory oxygen limits the reduction of NO, NO_2^- and NO_3^-. Reaction rates are designed to have a

517 dependency on the enzymes' level and biomass concentration with proper limiting/inhibiting terms.

518 Equation (12)(12) is used to describe the evolution of each biochemical species. The final system of

519 advective-diffusive-reactive equations is adapted from (Kampschreur et al., 2012):

$$\frac{\partial C_i}{\partial t} + \nabla \cdot (C_i \boldsymbol{u}) = -\nabla \cdot \left(D_i \nabla C_i - D_i \frac{1 - H_i}{\alpha + (1 - \alpha)H_i} C_i \nabla \alpha \right) + R_i,$$

$$i = suc, O_2, NO_3^-, NO_2^-, NO, N_2O \qquad\qquad in\ \Omega_\vartheta$$

$$R_{suc} = -(r_{suc,O_2} + r_{suc,NAP} + r_{suc,NIR} + r_{suc,NOR})$$

$$R_{O_2} = -1.2 r_{suc,O_2}$$

$$R_{NO_3^-} = -3.23 r_{suc,NAP}$$

$$R_{NO_2^-} = 3.23 r_{suc,NAP} - 6.45 r_{suc,NIR}$$

$$R_{NO} = 6.45 r_{suc,NIR} - 6.45 r_{suc,NOR}$$

$$R_{N_2O} = 3.23 r_{suc,NOR}$$

$$r_{suc,O_2} = \mu_{max} C_{bio} \frac{C_{O_2}}{K_{O_2}\left(1 + \frac{C_{NO}}{K_{I,NO,O_2}}\right) + C_{O_2}}$$

$$r_{suc,NAP} = \mu_{max} C_{bio} \xi_{sat,NAP} \frac{C_{NO_3}}{K_{NO_3} + C_{NO_3}} \frac{K_{I,O_2,NAP}^{nNAP}}{K_{I,O_2,NAP}^{nNAP} + C_{O_2}^{nNAP}}$$

$$r_{suc,NIR} = \mu_{max} C_{bio} \xi_{sat,NIR} \frac{C_{NO_2}}{K_{NO_2} + C_{NO_2}} \frac{K_{I,O_2,NIR}^{nNIR}}{K_{I,O_2,NIR}^{nNIR} + C_{O_2}^{nNIR}}$$

$$r_{suc,NOR} = \mu_{max} C_{bio} \xi_{sat,NOR} \frac{C_{NO}^2}{\left[C_{NO}\left(1 + \frac{C_{NO}}{K_{I,NO}}\right) + K_{NO}\right]^2} \frac{K_{I,O_2,NOR}}{K_{I,O_2,NOR} + C_{O_2}}$$

$$\frac{d\xi_{sat,NAP}}{dt} = v_{m,NAP} \frac{C_{NO_3}}{K_{NO_3,NAP} + C_{NO_3}} \frac{K_{I,O_2,NAP}}{K_{I,O_2,NAP} + C_{O_2}} (1 - \xi_{sat,NAP})$$

$$\frac{d\xi_{sat,NIR}}{dt} = v_{m,NIR} \frac{C_{NO_2}}{K_{NO_2,NIR} + C_{NO_2}} (1 - \xi_{sat,NIR})$$

$$\frac{d\xi_{sat,NOR}}{dt} = v_{m,NOR} \frac{C_{NO}}{K_{NO,NOR} + C_{NO}} (1 - \xi_{sat,NOR})$$

$$\frac{dC_{bio}}{dt} = 2.2 r_{suc,O_2} + 1.8(r_{suc,NAP} + r_{suc,NIR} + r_{suc,NOR})$$

520 The full list of modelling parameters used for this study can be found in the Table S.2 (see Supplementary
521 Information).

522 Reactive transport simulations were performed until a quasi-steady state was achieved. This was
523 characterized by all chemical species concentrations reaching a steady-state as determined by the
524 degradation activity of the given distribution of microorganisms. Since microbial growth takes place at
525 much larger time scales than the pore-scale transport processes no significant growth takes place during
526 the simulated time period and shown results are nearly identical to the initial conditions. Simulation

527 results show that the presence of air in this two-phase system affects the distribution of biochemical

528 species. Air, as the non-wetting phase, occupies the central part of the pore space while the aqueous phase

529 is expected to cover the corners and crevices (Figure 6Figure 6, a). For oxygen with $H_{O_2} = 31$ a higher

530 concentration is observed in the air compared to that of the adjacent aqueous phase (Figure 6Figure 6, d).

531 An analysis of how the volatility of a tracer compound may affect its residence time in the porous

532 medium is given in the Supplementary Information. Since the biomass is only present on the grain

533 surfaces (Figure 6Figure 6, b), oxygen, nitrate and succinate deplete as the microbially-mediated reactions

534 only at these micro-locations. Fresh oxygen and nitrate thus need to diffuse from the bulk (either from the

535 aqueous phase or the air) to the reactive sites. The regions with high (i.e. not degraded) succinate

536 concentrations are compatible with low concentration regions of oxygen and nitrate, i.e. the reactions are

537 limited by the bioavailable oxygen and nitrate (Figure 6Figure 6, b-e). Finally, all three enzymes have an

538 increased abundance in anaerobic regions with an active biomass (saturation map of nitrate reductase

539 enzyme is shown in Figure 6Figure 6, e). While the saturation of nitrate reductase enzyme grows linearly

540 with time (until 0.25 s), the rate at which the nitrite and NO reductase enzymes ($\xi_{sat,NIR}$ and $\xi_{sat,NOR}$

541 respectively) growth grow is rather slow for the very beginning of the simulation (until ~0.2 s), but it

542 surges exponentially afterward. A spatially integrated assessment of the degradation processes showed

543 that for the presented example 99% of the total succinate degradation is attributed to aerobic respiration

544 while a trivial amount is attributed to the three anaerobic processes (nitrate reduction, nitrite reduction and

545 NO reductions).

546 The presented results highlight the ability of the model to combine a high-resolution simulation of multi-

547 phase flow and transport processes with the simulation of complex biogeochemical processes. This allows

548 for a realistic simulation of the pore-scalemicro-scale distribution of reactive processes and for the

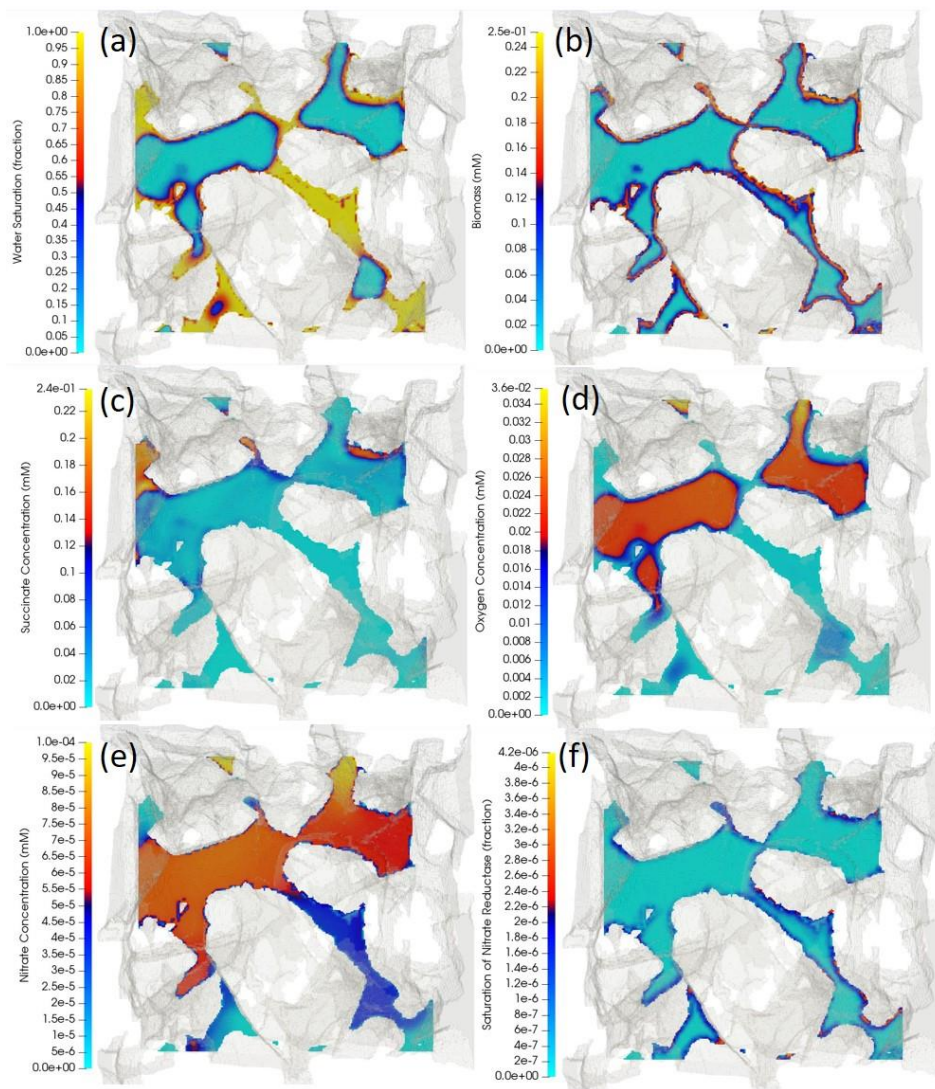549 derivation of an accurate aggregated description of these processes.

550

Figure 6Cross-sectional view of the three dimensional porous medium. The cutting plane is arbitrary cutting through the middle of the porous structure, meaning at some locations, the phases are continuous perpendicular to the plane. The opaque grayish background represents the 3D porous structure that is extracted and digitized from a µ-CT image. The colored surfaces are obtained by running a cutting plane through the middle of the sample and perpendicular to the z-axis. The distribution of (a) water-content fraction (i.e. water volume fraction), (b) biomass, (c) succinate, (d) oxygen, (e) nitrate and (f) nitrate reductase enzyme are respectively depicted with having yellow color indicating highest value and light blue as the lowest value. With air as the non-wetting phase, it is expected to fill in the middle of the pore space where capillary pressure is lower while water, as the wetting phase, is expected to occupy the corners (figure a). A high volatility constant for oxygen enforces to have higher concentrations of oxygen in the air compared to that of aqueous phase adjacent to the water-air interface. Cross-sectional view of

25

568 As it can be seen from ~~Figure 6~~Figure 6, our model can be used (among other options) to identify clusters

569 in which succinate is most and least depleted. This would ease the process of analyzing the results by

570 isolating the parameters that are boosting/limiting the degradation of the carbon source. 3D visualization

571 of the oxygen and succinate distributions can be found in ~~(~~Golparvar, 2022~~)~~.

4. Conclusion and future remarks

573 In this paper, we have presented a newly developed modelling framework for simulating reactive

574 transport processes in real porous soil structures obtained from µ-CT images under unsaturated

575 conditions. The successful application of various benchmark test showed the model's accuracy in the

576 simulation of 1) the movement of water and air phase in variably saturated conditions via the enhanced

577 algebraic Volume of Fluid method (Raeini et al., 2012) coupled with the Navier Stokes equation, 2) the

578 transport of different species in both phases by the full advective-diffusive transport equation, and finally

579 3) using the operator splitting technique, an arbitrary set of biogeochemical reactions solved externally by

580 the Biogeochemical Reaction Network Simulator and communicated back into the main solver.

581 The presented model provides a novel and unique combination of pore-scale simulations of two-phase

582 flow, transport of dissolved and volatile species and their reactive transformations. This makes it an

583 accurate and powerful tool for the simulation of soil systems or other unsaturated porous media and of the

584 reactive transport processes therein. While developed with the aim for simulating biogeochemical

585 processes in soils the model is equally applicable for simulating other abiotic reactive processes coupled

586 to the dynamics of flow and transport in variably saturated pore structures of arbitrary geometry. Our

587 modelling framework is properly designed for simulating biogeochemical processes such as carbon-

588 nitrogen-sulfur-phosphorus cycles in soil as well as mixing and migration of contaminants in both

589 unsaturated soil and water aquifers. It comes with the benefit of explicit recognition of the soil structure

590 (i.e. using the 3D structure as close to the original shape as possible with the least amount of

591 simplifications/modifications), phase dynamics/distributions and the capability of designing the complete

592 redox reactions necessary for a given process in a straightforward fashion. It is best suitable for running

593 pre-pilot tests as feasibility scenarios where the stakes for the success of the project are high. Also, our

594 model provides the best tool for designing hypothetical experiments that are hard (if not impossible) to

595 implement experimentally (e.g. a specific distribution of biomass/reactants within the domain, or

26

596 variation of specific properties of reactive compound and/or the porous matrix). Furthermore, the high
597 resolution modelling results provided by this model support the upscaling of reactive-transport process
598 description from the pore to the continuum scale and from the process to the observation scale,
599 respectively.

600 Although the current version of our numerical model is already covering a wide range of bio-physio-
601 chemical properties of the soil constituents, for having more realistic representation of multiphase,
602 multicomponent reactive transport in partially saturated porous media, few more factors still might be
603 considered in future developments of the model: 1) shrinkage/expanding of the air/aqueous phase due to
604 mass transfer of chemical species across fluid-fluid interface, 2) accounting for gas compressibility by
605 adding an equation of state for tracking changes of air volume/density under flowing condition, 3)
606 translating accumulated biomass on the grain surfaces into new flow-resistance components which would
607 potentially change the velocity streamlines (i.e. bioclogging), 4) changes of the grain surface structures
608 and of the associated solid-liquid interface due to mineral precipitation/dilution or due to
609 accumulation/depletion of solid organic material, and 5) chemotactic behavior of the microbial species,
610 and 6) osmotic forces and electro-migration. Due to its modular structure, such features can be relatively
611 easily included into future upgrades of our model. .

5.   Acknowledgements

6.   Code and data availability

616 The source codes, benchmark and demonstration cases along with instruction for installing and running
617 each case that are presented in this paper, are archived at https://github.com/amirgolp/P3D-BRNS_DOI:
618 10.5281/zenodo.6301317.

7.   Author contributions

620 AR was responsible for model/software curation, validation and visualization. Conceptualization and
621 methodology development were managed by AR, MK, and MT. Writing the original manuscript was
622 handled by AR while all authors contributed to the revision and curation of the final draft. The entire
623 work is supervised by MT.

8.   Competing interests

625 The authors declare that they have no conflict of interest.

9.   References

Aguilera, D. R., Jourabchi, P., Spiteri, C., and Regnier, P.: A knowledge-based reactive transport approach for the simulation of biogeochemical dynamics in Earth systems, Geochemistry Geophysics Geosystems, 6, Q07012, 10.1029/2004gc000899, 2005.

Albadawi, A., Donoghue, D. B., Robinson, A. J., Murray, D. B., and Delauré, Y. M. C.: Influence of surface tension implementation in Volume of Fluid and coupled Volume of Fluid with Level Set methods for bubble growth and detachment, International Journal of Multiphase Flow, 53, 11-28, https://doi.org/10.1016/j.ijmultiphaseflow.2013.01.005, 2013.

Baveye, P. C., Palfreyman, J., and Otten, W.: Research Efforts Involving Several Disciplines: Adherence to a Clear Nomenclature Is Needed, Water Air Soil Poll, 225, ARTN 1997

10.1007/s11270-014-1997-7, 2014.

Baveye, P. C., Baveye, J., and John Gowdy, J.: Soil "Ecosystem" Services and Natural Capital: Critical Appraisal of Research on Uncertain Ground., Frontiers in Environmetal Science, 4, 41, 10.3389/fenvs.2016.00041, 2016

Baveye, P. C., Otten, W., Kravchenko, A., Balseiro-Romero, M., Beckers, É., Chalhoub, M., Darnault, C., Eickhorst, T., Garnier, P., and Hapca, S.: Emergent properties of microbial activity in heterogeneous soil microenvironments: different research approaches are slowly converging, yet major challenges remain, Frontiers in microbiology, 9, 1929, 2018.

Beun, J., Verhoef, E., Van Loosdrecht, M., and Heijnen, J.: Stoichiometry and kinetics of poly-β-hydroxybutyrate metabolism under denitrifying conditions in activated sludge cultures, Biotechnology and Bioengineering, 68, 496-507, 2000.

Bird, R. B.: Transport phenomena, Appl. Mech. Rev., 55, R1-R4, 2002.

Blunt, M. J.: Multiphase flow in permeable media: A pore-scale perspective, Cambridge University Press, 2017.

Brackbill, J. U., Kothe, D. B., and Zemach, C.: A continuum method for modeling surface tension, J Comput Phys, 100, 335-354, https://doi.org/10.1016/0021-9991(92)90240-Y, 1992.

Centler, F., Shao, H., De Biase, C., Park, C.-H., Regnier, P., Kolditz, O., and Thullner, M.: GeoSysBRNS-A flexible multidimensional reactive transport model for simulating biogeochemical subsurface processes, Computers & Geosciences, 36, 397-405, 10.1016/j.cageo.2009.06.009, 2010.

Cirpka, O. A., and Valocchi, A. J.: Two-dimensional concentration distribution for mixing-controlled bioreactive transport in steady state, Advances in Water Resources, 30, 1668-1679, 10.1016/j.advwatres.2006.05.022, 2007a.

Cirpka, O. A., and Valocchi, A. J.: Two-dimensional concentration distribution for mixing-controlled bioreactive transport in steady state, Advances in Water Resources, 30, 1668-1679, https://doi.org/10.1016/j.advwatres.2006.05.022, 2007b.

Cirpka, O. A., and Valocchi, A. J.: Reply to comments on "Two-dimensional concentration distribution for mixing-controlled bioreactive transport in steady state" by H. Shao et al, Advances in Water Resources, 32, 298-301, 10.1016/j.advwatres.2008.10.018, 2009.

Danckwerts, P. V., and Lannus, A.: Gas-liquid reactions, Journal of The Electrochemical Society, 117, 369C, 1970.

Gharasoo, M., Centler, F., Regnier, P., Harms, H., and Thullner, M.: A reactive transport modeling approach to simulate biogeochemical processes in pore structures with pore-scale heterogeneities, Environmental modelling & software, 30, 102-114, 2012.

Golparvar, A., Kästner, M., and Thullner, M.: Pore-scale modeling of microbial activity: What we have and what we need, Vadose Zone Journal, 20, e20087, https://doi.org/10.1002/vzj2.20087, 2021.

Golparvar, A.: Movies. figshare, 2022.

672 Graham, E., Grandy, S., and Thelen, M.: Manure effects on soil organisms and soil quality, Emerging
673 Issues in Animal Agriculture. Michigan State University Extension, 2014.
674 Graveleau, M., Soulaine, C., and Tchelepi, H. A.: Pore-Scale Simulation of Interphase Multicomponent
675 Mass Transfer for Subsurface Flow, Transport Porous Med, 120, 287-308, 10.1007/s11242-017-0921-1,
676 2017.
677 Greenshields, C. J.: OpenFOAM user guide, OpenFOAM Foundation Ltd, version, 3, 47, 2015.
678 Haroun, Y., Legendre, D., and Raynal, L.: Volume of fluid method for interfacial reactive mass transfer:
679 Application to stable liquid film, Chemical Engineering Science, 65, 2896-2909,
680 https://doi.org/10.1016/j.ces.2010.01.012, 2010.
681 Hirt, C. W., and Nichols, B. D.: Volume of fluid (VOF) method for the dynamics of free boundaries, J
682 Comput Phys, 39, 201-225, https://doi.org/10.1016/0021-9991(81)90145-5, 1981.
683 Issa, R. I.: Solution of the implicitly discretised fluid flow equations by operator-splitting, J Comput Phys,
684 62, 40-65, 1986.
685 Kampschreur, M. J., Kleerebezem, R., Picioreanu, C., Bakken, L. R., Bergaust, L., de Vries, S., Jetten, M. S.,
686 and Van Loosdrecht, M.: Metabolic modeling of denitrification in Agrobacterium tumefaciens: a tool to
687 study inhibiting and activating compounds for the denitrification pathway, Frontiers in microbiology, 3,
688 370, 2012.
689 Kuzyakov, Y., and Blagodatskaya, E.: Microbial hotspots and hot moments in soil: Concept & review, Soil
690 Biology and Biochemistry, 83, 184-199, https://doi.org/10.1016/j.soilbio.2015.01.025, 2015.
691 Li, X. Y., Huang, H., and Meakin, P.: A three-dimensional level set simulation of coupled reactive
692 transport and precipitation/dissolution, Int J Heat Mass Tran, 53, 2908-2923,
693 10.1016/j.ijheatmasstransfer.2010.01.044, 2010.
694 Meakin, P., and Tartakovsky, A. M.: Modeling and simulation of pore-scale multiphase fluid flow and
695 reactive transport in fractured and porous media, Reviews of Geophysics, 47, 2009.
696 Meile, C., and Scheibe, T. D.: Reactive Transport Modeling of Microbial Dynamics, Elements, 15, 111-
697 116, 10.2138/gselements.15.2.111, 2019.
698 Nick, H. M., Raoof, A., Centler, F., Thullner, M., and Regnier, P.: Reactive dispersive contaminant
699 transport in coastal aquifers: numerical simulation of a reactive Henry problem, Journal of Contaminant
700 Hydrology, 145, 90-104, 10.1016/j.jconhyd.2012.12.005, 2013.
701 Parkhurst, D. L., and Appelo, C. A. J.: User's guide to PHREEQC (Version 2) : a computer program for
702 speciation, batch-reaction, one-dimensional transport, and inverse geochemical calculations, Report 99-
703 4259, 1999.
704 Patankar, S. V., and Spalding, D. B.: A calculation procedure for heat, mass and momentum transfer in
705 three-dimensional parabolic flows, Int J Heat Mass Tran, 15, 1787-1806, https://doi.org/10.1016/0017-
706 9310(72)90054-3, 1972.
707 Popinet, S.: An accurate adaptive solver for surface-tension-driven interfacial flows, J Comput Phys, 228,
708 5838-5866, https://doi.org/10.1016/j.jcp.2009.04.042, 2009.
709 Raeini, A. Q., Blunt, M. J., and Bijeljic, B.: Modelling two-phase flow in porous media at the pore scale
710 using the volume-of-fluid method, J Comput Phys, 231, 5653-5668, 2012.
711 Regnier, P., O'Kane, J. P., Steefel, C. I., and Vanderborght, J. P.: Modeling complex multi-component
712 reactive-transport systems: towards a simulation environment based on the concept of a Knowledge
713 Base, Applied Mathematical Modelling, 26, 913-927, https://doi.org/10.1016/S0307-904X(02)00047-1,
714 2002.
715 Sander, R.: Compilation of Henry's law constants (version 4.0) for water as solvent, Atmos. Chem. Phys.,
716 15, 4399-4981, 10.5194/acp-15-4399-2015, 2015.
717 Scardovelli, R., and Zaleski, S.: DIRECT NUMERICAL SIMULATION OF FREE-SURFACE AND INTERFACIAL
718 FLOW, Annual Review of Fluid Mechanics, 31, 567-603, 10.1146/annurev.fluid.31.1.567, 1999.

719 Schlüter, S., Zawallich, J., Vogel, H.-J., and Dörsch, P.: Physical constraints for respiration in microbial
720 hotspots in soil and their importance for denitrification, Biogeosciences Discussions, 1-31, 2019.
721 Schmidt, H., Vetterlein, D., Köhne, J. M., and Eickhorst, T.: Negligible effect of X-ray μ-CT scanning on
722 archaea and bacteria in an agricultural soil, Soil Biology and Biochemistry, 84, 21-27, 2015.
723 Steefel, C., and MacQuarrie, K.: Approaches to modeling of reactive transport in porous media, Reviews
724 in Mineralogy & Geochemistry, 34, 85-129, 1996.
725 Steefel, C. I., Appelo, C. A. J., Arora, B., Jacques, D., Kalbacher, T., Kolditz, O., Lagneau, V., Lichtner, P. C.,
726 Mayer, K. U., Meeussen, J. C. L., Molins, S., Moulton, D., Shao, H., `imonek, J., Yabusaki, S. B., and Yeh, G.
727 T.: Title Reactive transport codes for subsurface environmental simulation, 2015a,
728 Steefel, C. I., Appelo, C. A. J., Arora, B., Jacques, D., Kalbacher, T., Kolditz, O., Lagneau, V., Lichtner, P. C.,
729 Mayer, K. U., Meeussen, J. C. L., Molins, S., Moulton, D., Shao, H., Šimůnek, J., Spycher, N., Yabusaki, S.
730 B., and Yeh, G. T.: Reactive transport codes for subsurface environmental simulation, Computational
731 Geosciences, 19, 445-478, 10.1007/s10596-014-9443-x, 2015b.
732 Thullner, M., Van Cappellen, P., and Regnier, P.: Modeling the impact of microbial activity on redox
733 dynamics in porous media, Geochim Cosmochim Ac, 69, 5005-5019, 10.1016/j.gca.2005.04.026, 2005.
734 Thullner, M., Regnier, P., and Van Cappellen, P.: Modeling Microbially Induced Carbon Degradation in
735 Redox-Stratified Subsurface Environments: Concepts and Open Questions, Geomicrobiology Journal, 24,
736 139-155, 10.1080/01490450701459275, 2007.
737 Thullner, M.: Comparison of bioclogging effects in saturated porous media within one- and two-
738 dimensional flow systems, Ecological Engineering, 36, 176-196, 10.1016/j.ecoleng.2008.12.037, 2010.
739 Thullner, M., and Regnier, P.: Microbial Controls on the Biogeochemical Dynamics in the Subsurface,
740 Reviews in Mineralogy and Geochemistry, 85, 265-302, 10.2138/rmg.2019.85.9, 2019.
741 Tian, Z. W., and Wang, J. Y.: Lattice Boltzmann simulation of biofilm clogging and chemical oxygen
742 demand removal in porous media, Aiche J, 65, UNSP e16661

743 10.1002/aic.16661, 2019.
744 van Leer, B.: Towards the ultimate conservative difference scheme. V. A second-order sequel to
745 Godunov's method, J Comput Phys, 32, 101-136, https://doi.org/10.1016/0021-9991(79)90145-1, 1979.
746 Whitaker, S.: The method of volume averaging, Springer Science & Business Media, 2013.
747 White, A. F., and Brantley, S. L.: The effect of time on the weathering of silicate minerals: why do
748 weathering rates differ in the laboratory and field?, Chem Geol, 202, 479-506,
749 https://doi.org/10.1016/j.chemgeo.2003.03.001, 2003.
750 Yan, Z. F., Liu, C. X., Todd-Brown, K. E., Liu, Y. Y., Bond-Lamberty, B., and Bailey, V. L.: Pore-scale
751 investigation on the response of heterotrophic respiration to moisture conditions in heterogeneous
752 soils, Biogeochemistry, 131, 121-134, 10.1007/s10533-016-0270-0, 2016.

753